Journal of Solid State Chemistry 293 (2021) 121838

Contents lists available at ScienceDirect

Journal of Solid State Chemistry

journal homepage: www.elsevier.com/locate/jssc

Revisiting the thermal and chemical expansion and stability of $La_{0.6}Sr_{0.4}FeO_{3-\delta}$

Christopher de Leeuwe [a,b], Wenting Hu [a], Dragos Neagu [a,c], Evangelos I. Papaioannou [a], Stevin Pramana [a], Brian Ray [a], John S.O. Evans [d], Ian S. Metcalfe [a,*]

[a] School of Engineering, Newcastle University, Newcastle upon Tyne, NE1 7RU, UK
[b] Department of Chemical Engineering and Analytical Science, The University of Manchester, Manchester, M1 3AL, UK
[c] Department of Chemical and Process Engineering, The University of Strathclyde, Glasgow, G1 1XJ, UK
[d] Department of Chemistry, Durham University, Durham, DH1 3LE, UK

ARTICLE INFO

Keywords:
Strontium-doped lanthanum ferrite
Chemical expansivity
Thermal expansivity
Mixed ionic electronic conductor
Membrane
SOFC cathode
Chemical looping

ABSTRACT

The thermal and chemical expansivity of $La_{1-x}Sr_xFeO_{3-\delta}$ ($x = 0.4$) was measured using *in situ* powder neutron and synchrotron X-ray diffraction at temperatures between 932 K and 1170 K and oxygen partial pressures, P_{O_2}, between 10^{-19} bar and 0.1 bar, giving a wide range of oxygen non-stoichiometry from $\delta = 0.05$ to 0.22. Changes in δ were measured independently using gas analysis. This P_{O_2} and temperature range covers the material's use as a chemical looping oxygen carrier, a sensor material and in solid oxide fuel cells. Thermal and chemical expansivities were found to be dependent on the oxygen non-stoichiometry, δ. For $\delta < 0.2$ and $T = 932$–1050 K, the linear thermal expansivity was $5.72(4) \times 10^{-5}$ Å/K and the linear chemical expansivity was 0.144(9) Å per unit change in δ. For $\delta > 0.2$ and $T = 973$–1173 K, the linear thermal expansivity increases to $6.18(8) \times 10^{-5}$ Å/K. For $\delta > 0.2$, the linear chemical expansivity varies with both δ and temperature.

1. Introduction

Perovskite oxides such as strontium-doped lanthanum ferrite, $La_{1-x}Sr_xFeO_{3-\delta}$, have been investigated for use in various functional devices such as solid oxide fuel cell (SOFC) cathodes [1–4], oxygen permeation membranes [5], and chemical sensors [6–8] due to their high conductivity of both electrons and oxyide ions. More recently, these materials have been studied as oxygen carriers for chemical looping combustion (CLC) and chemical looping H_2 production [9–11]. Both CLC and chemical-looping H_2 production have the potential to reduce the cost of separating CO_2 from gaseous product streams, negating the need for energy intensive processes like CO_2 removal using amine columns (for CO_2 capture from power plants) or pressure swing adsorption (for CO_2 separation from H_2 product streams) [12].

Repeated oxidation and reduction of a crystalline oxygen carrier material (OCM) can cause relatively large changes in its unit cell parameters and can lead to decreased operational lifetime owing to decreased mechanical integrity. Bishop et al. [13] reviewed the effect of structural changes of a material based on changing chemical conditions. They found that the chemical expansivity can have a direct effect on the elastic modulus of the material and its ionic and electronic conductivity. Understanding the magnitude of the shifts in unit cell parameter due to chemical changes of the material is, therefore, important for the design of functional devices. Thermal stresses have a similar effect to chemical stresses, compromising the mechanical integrity of a material and causing cracks [14]. Therefore, knowledge of the phase stability and the chemical and thermal expansivities, under relevant operation conditions underpins the appropriate design and implementation of functional devices.

The thermal and chemical expansivities of a material describe how the unit cell parameter changes as a function of temperature and the material's composition. For a cubic $ABO_{3-\delta}$ structure, the expansivities are defined by Equations (1) and (2).

$$\text{Thermal expansivity} = \left(\frac{\partial a}{\partial T}\right)_{\delta} \quad (1)$$

* Corresponding author.
E-mail address: ian.metcalfe@ncl.ac.uk (I.S. Metcalfe).

https://doi.org/10.1016/j.jssc.2020.121838
Received 10 June 2020; Received in revised form 22 October 2020; Accepted 26 October 2020
Available online 6 November 2020

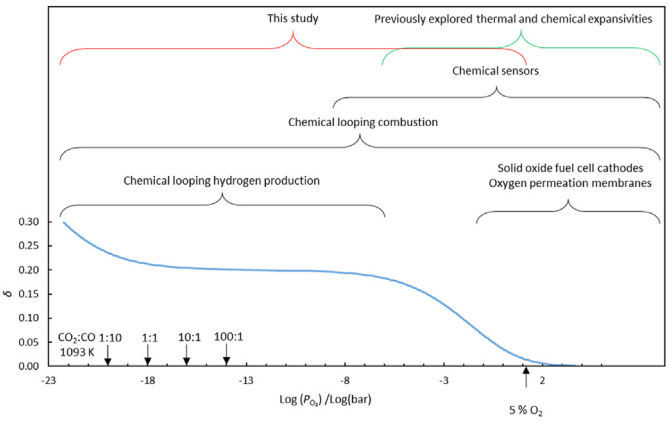

Fig. 1. A plot of δ as a function of P_{O_2} at 1093 K highlighting where the thermal and chemical expansivity of $La_{0.6}Sr_{0.4}FeO_{3-\delta}$ has been previously reported. The P_{O_2} of several CO_2:CO buffer gasses of interest are also marked [21]. The range of p_{O_2} needed for different applications are highlighted [1–8].

$$\text{Chemical expansivity} = \left(\frac{\partial a}{\partial \delta}\right)_T \quad 2$$

where a is the cubic unit cell parameter, T is the temperature and δ represents the deviation from stoichiometry in moles of oxygen per mole of perovskite.

This study focused on the $x = 0.4$ member of the series $La_{1-x}Sr_xFeO_{3-\delta}$. $La_{0.6}Sr_{0.4}FeO_{3-\delta}$ is of particular interest as it remains single phase at the oxygen partial pressures (P_{O_2}) and temperatures of interest to chemical looping and sensor technologies (10^{-23} to 10^{1} bar and 500–1200 K). $La_{0.6}Sr_{0.4}FeO_{3-\delta}$ has a rhombohedrally distorted perovskite structure at room temperature. As the temperature increases, it transforms to a cubic structure, with the exact temperature of the transition depending on δ [15].

$La_{0.6}Sr_{0.4}FeO_{3-\delta}$ is well studied in the literature, and this includes the investigation of the oxygen non-stoichiometry over a wide range of temperatures and P_{O_2}, and the thermal and chemical expansivity over a smaller range of temperatures and P_{O_2} [1,2,16–20]. The expansivity studies concentrated on SOFC cathode applications so that the range of P_{O_2} where the thermal and chemical expansivity were investigated was limited to $>10^{-7}$ bar, as shown in Fig. 1.

The oxygen non-stoichiometry of strontium-doped lanthanum ferrite has been explained using a point defect model [1,2,20], and the acceptor (Sr_{La}' in Kröger–Vink notation) compensation mechanism is known to change as a function of P_{O_2}. In the stoichiometric state (*i.e.* $\delta = 0$), Sr^{2+} is compensated by holes in the form of Fe^{4+} ($Fe_{Fe}^{\bullet}$). As P_{O_2} is lowered, oxygen vacancies form and the proportion of Fe^{4+} content decreases (*i.e.* an increasing amount of oxygen vacancies, $V_O^{\bullet\bullet}$, offset by a decreasing amount of $Fe_{Fe}^{\bullet}$ are present). This is followed by a plateau at $\delta = x/2$ (*i.e.* $\delta = 0.2$ for $La_{0.6}Sr_{0.4}FeO_{3-\delta}$) where vacancy compensation dominates over a wide P_{O_2} range. Finally, at low P_{O_2} further reduction creates additional oxygen vacancies and electrons in the form of reduced Fe^{2+} (Fe_{Fe}').

Taylor et al. [11] used synchrotron XRD and neutron diffraction to study how the structure of different strontium-doped lanthanum ferrites changes during chemical looping combustion using CH_4 as the reducing agent and O_2 as the oxidising agent. This shows these materials' ability to regenerate when cycled and how they might change under these specific conditions. However, the lack of a well-defined P_{O_2} for the reduction step makes extraction of chemical and thermal expansivities impossible, limiting the insight this work can give to the other uses of $La_{0.6}Sr_{0.4}FeO_{3-\delta}$.

Chen and Grande [16] reported how the unit cell parameter of $La_{0.6}Sr_{0.4}FeO_{3-\delta}$ and other perovskites in the La–Sr series changed under two different gas environments, O_2 and N_2 (assumed to be a P_{O_2} of 5×10^{-5} bar). These experiments defined δ based on thermogravimetric (TG) data and an understanding of the relationship between P_{O_2} and δ. With only two P_{O_2}'s at a given temperature, extraction of both chemical and thermal expansion for a range of δ and temperatures is problematic. Additionally, the system was limited to a minimum P_{O_2} of 5×10^{-5} bar, significantly higher than that required for chemical looping combustion or hydrogen production (down to 10^{-22} bar). Kuhn et al. [20] conducted studies at a slightly less reducing condition (10^{-4}) using N_2/O_2 mixtures. The exact P_{O_2} was determined using zirconia sensors. This allowed them to separate the chemical and thermal expansivities of the material between 1 bar and 10^{-4} bar and up to a temperature of 1173 K. Both expansivities were found to be constant and independent of each other. The chemical expansivity was found to be 0.07773 Å per δ and the thermal expansivity was found to be 4.307×10^{-5} Å/K in the range of temperatures and P_{O_2} they studied. These values are used as the benchmark for comparison in this work.

While both the thermal and chemical expansivity of $La_{0.6}Sr_{0.4}FeO_{3-\delta}$ were found to be constant when $\delta > 0.2$ (where the transformation from Fe^{4+} to Fe^{3+} dominates) [20], it is expected that, due to the different oxidation states of Fe species present, the expansivities will be different when $\delta > 0.2$, where the transformation from Fe^{4+}/Fe^{3+} to Fe^{3+}/Fe^{2+} dominates [2].

In this work, *in situ* neutron and synchrotron X-ray powder diffraction studies were performed at temperatures between 932 K and 1170 K and P_{O_2} between 10^{-19} bar and 0.1 bar under continuous gas flow, to determine the thermal and chemical expansivity of $La_{0.6}Sr_{0.4}FeO_{3-\delta}$ over a wide range of oxygen non-stoichiometry from $\delta = 0.05$–0.22. The P_{O_2} range extends to much lower oxygen partial pressures than previously studied. This was coupled with analysis of the gas composition at the outlet of the system to determine the changes in δ caused by the different P_{O_2} and temperature conditions. The use of gas analysis also ensured that steady state was reached and that δ was well defined and corroborated by independent methods.

1. Experimental

1.1. Sample preparation

$La_{0.6}Sr_{0.4}FeO_{3-\delta}$ was synthesised using a Pechini-type method [22]. In order to produce 20 g of $La_{0.6}Sr_{0.4}FeO_{3-\delta}$, 23.38 g of $La(NO_3)_3{\cdot}6H_2O$ (Sigma Aldrich, 61520), 7.62 g of $Sr(NO_3)_2$ (Sigma Aldrich, 243426), 36.36 g of $Fe(NO_3)_3{\cdot}9H_2O$ (Sigma Aldrich, 216828) and 34.58 g of citric acid (Sigma Aldrich, 791725) were dissolved in 90 ml of deionised H_2O. 13.10 g of ethylene glycol (Sigma Aldrich, 243426) was then added. The mixture was mixed for 5 min before drying at 333 K for 48 h. The resulting orange cake was lightly crushed and placed in an alumina crucible and heated to 1323 K at 1 K min^{-1} and held for 18 h. The resulting powder was then sieved to select particles between 80 and 160 μm in size.

The sample was analysed via synchrotron X-ray powder diffraction at room temperature and atmospheric pressure and found to be a perovskite in the space group $R\bar{3}c$. The comparison between the observed and calculated diffraction patterns can be found in Supplementary Information Fig. S2.

1.2. Flow systems and gas analysis

A schematic diagram of the reactor systems used in this work are shown in Fig. 2. Gas flow was controlled using Brooks flow meters which give a flowrate controllable from 0 to 100 ml/min (STP) with an accuracy of 1% of the set point. A manifold was used to allow rapid switching between gasses. The gasses attached to the system were from premixed cylinders supplied by BOC, a complete list of the gas compositions used is given in Table 1. Throughout the paper CO_2, CO and Ar gas mixtures are referred to by the CO_2:CO ratio without reference to the inert Ar.

Two different reactors were used for the *in situ* diffraction

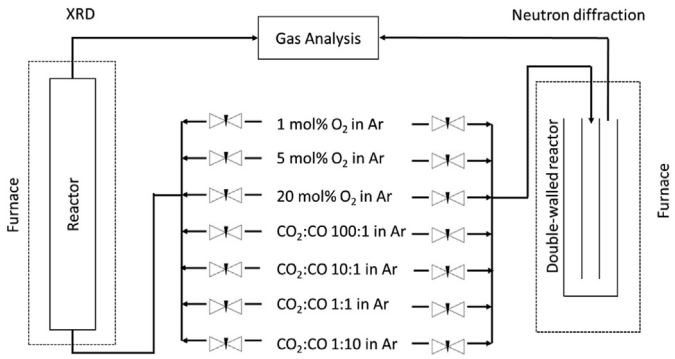

Fig. 2. A schematic diagram of the reactor systems used in this study.

Table 1
Gas environments used to determine expansivities, the remaining mass percentages are Ar. Mole fractions were certified to be within 5% of the quoted values by BOC.

Gas	CO_2:CO ratio	P_{O_2} at 1093 K and 1 bara (bar)
1 mol% O_2	N/A	0.01
5 mol% O_2	N/A	0.05
20 mol% O_2	N/A	0.20
5 mol% CO_2 with 0.05 mol% CO	100:1	1.23×10^{-14}
5 mol% CO_2 with 0.5 mol% CO	10:1	1.23×10^{-16}
2.5 mol% CO_2 with 2.5 mol% CO	1:1	1.23×10^{-18}
0.5 mol% CO_2 with 5 mol% CO	1:10	1.23×10^{-20}

experiments. For the neutron experiments we used a double-walled reactor made from 2 mm wall thickness silica tubing. This allowed gas flow down through a central 10 mm internal diameter (id) tube holding the reactor bed supported on sintered silica, and exit via an 18 mm id outer tube to the top of the reactor. This design fits inside the Riso furnace [23] supplied by ISIS Neutron and Muon Source and allows both inlet and outlet gases to be fed to the top of the reactor. 2.95 g of $La_{0.6}Sr_{0.4}FeO_{3-\delta}$, sieved to 80–160 μm, was placed in the reactor giving a bed height of 30 mm. Temperature was measured with a K-type thermocouple placed inside the reactor, 10 mm above the sample.

The silica reactor used for the X-ray diffraction experiments had an id of 4 mm. 0.44 g of $La_{0.6}Sr_{0.4}FeO_{3-\delta}$ (sieved to 80–160 μm) was intimately mixed with 0.09 g of Y_2O_3 (sieved to 10–20 μm) and placed in the reactor. The sample had a bed height of 25 mm and was held in place using silica wool. The furnace detailed by Metcalfe et al. [24] was used to heat the sample. Y_2O_3 was used as an internal temperature reference due to its inertness to the CO, CO_2 and O_2 [25], and the fact that its Bragg peaks do not overlap with major peaks of $La_{0.6}Sr_{0.4}FeO_{3-\delta}$. The temperature could only be derived from the internal standard during analysis, so thermocouple measurements outside the reactor were used during experiments to ensure thermal equilibrium had been achieved.

Outlet gas analysis was carried out using a quadrupole mass spectrometer (QGA, Hiden Analytical). This measured the mole fraction of O_2, CO, CO_2 and Ar present in the outlet gas. The outlet gas composition was used to determine when equilibrium between the gas and solid had been reached after a change in the inlet gas composition or in reactor temperature. Equilibrium was defined as when the outlet gas mole fractions for all reactive gasses were within 0.05 mol% of the inlet values for over 180 s and when the temperature variation was less than 1 K over 60 s based on thermocouple readings.

By integrating the difference between the inlet and outlet gas composition between the initiation of a change and when the sample reached a new equilibrium state, it is possible to calculate the change in oxygen content of the solid and therefore the change in δ associated with that change in temperature or gas composition. A full description of the steps involved in the gas analysis can be found in SI Section 3.

1.3. High temperature in situ neutron diffraction under different P_{O_2}

Neutron powder diffraction data were collected using the High Resolution Powder Diffractometer (HRPD) at the ISIS time-of-flight (tof) neutron source of the Rutherford Appleton laboratory. A tof range of 10–110 ms was chosen (d-spacing ranges approx. 0.4–3.3 and 0.3–2.2 Å for the 90° and backscattering detectors, respectively).

Data were collected on an as-prepared sample of $La_{0.6}Sr_{0.4}FeO_{3-\delta}$ as it was heated from 298 K to 1098 K in 25 K steps under a gas environment of 1:1 CO_2:CO in Ar at atmospheric pressure ($P_{O_2} = 1.23 \times 10^{-18}$ bar at 1093 K if equilibrium is achieved). Each scan was for a duration of 5 min to maximise the number of temperatures that could be measured.

Following these measurements, data were collected on the same sample at different temperatures between 973 K and 1173 K in five different flowing gas environments at atmospheric pressure (4 CO_2/CO mixtures in Ar and 5% O_2 in Ar), corresponding to the P_{O_2} detailed in Table 1. The system was given 30 min to equilibrate at each temperature and gas environment. Data were recorded in five 20 μAh (~30 min) blocks once equilibrium was achieved. Rietveld fitting of separate 20 μAh blocks recorded under the same conditions gave consistent results within experimental uncertainty, confirming the sample had fully equilibrated. Individual data sets were therefore summed for use in the final analysis.

1.4. High temperature in situ X-ray diffraction

High temperature synchrotron X-ray diffraction (XRD) was used to determine expansivities to compare with those reported in previous work and our neutron diffraction experiments. This was done to check for systematic errors in either experiment. Experiments were carried out on ID22 at the European Synchrotron Radiation Facility (ESRF) using the multi-analyser detector [26]. Diffraction patterns were recorded from 9° to 17° in 2θ at a scan speed of 2° per minute with a wavelength of 0.3542 Å (35 keV), calibrated using a silicon standard. The sample temperature was extracted using the cell parameter data of Y_2O_3 published by Swamy et al. [27] and Taylor et al. [28] via the expression:

$$T = \frac{-B + (B^2 - 4 \times A(C - a_{Y_2O_3}))^{0.5}}{2A}, \quad 3$$

$A = 1.29340 \times 10^{-8}$ Å$/K^2$, $B = 6.46011 \times 10^{-5}$ Å$/K$, $C = 10.58733218$ ÅA, B and C are empirical constants, T is the temperature of the sample and $a_{Y_2O_3}$ is the measured unit cell parameter.

The dependence of the unit cell parameter of $La_{0.6}Sr_{0.4}FeO_{3-\delta}$ on thermal and chemical changes was studied between 920 K and 1060 K for P_{O_2} of 0.2–0.01 bar using 20%, 5% and 1% O_2 in Ar. Experiments were also conducted for P_{O_2} in the range 10^{-15}–10^{-19} bar using CO_2:CO ratios of 10:1, 1:1 and 1:10 at temperatures from 1065 K to 1090 K.

1.5. Rietveld fitting strategy

Rietveld fitting of the diffraction data was performed using TOPAS v7 [29,30]. Unit cell parameters, oxygen site occupancy, atomic displacement parameters (anisotropic for oxygen) and sample contributions to the peak shape were refined. The neutron background was fitted by including a function describing the measured background of the empty sample container, along with additional terms of a Chebyshev polynomial. Sample peak shape contributions were described by convolving terms describing isotropic size and strain broadening onto an instrumental peak shape determined empirically from a Si (neutron) or LaB_6 (synchrotron) standard. The site occupancies of La, Sr and Fe were kept constant at 0.6, 0.4 and 1.0 respectively.

For the neutron diffraction data collected on warming from 298 to 1098 K under a reducing 1:1 CO_2:CO atmosphere, a rhombohedral model ($R\bar{3}c$) was used to fit experimental data at all temperatures, and cell parameters converted to pseudo-cubic values for plotting. Various structural models were investigated to determine the oxygen content.

Allowing the oxygen site occupancy to vary led to an overall content of 2.957(6) per formula unit at temperatures below 623 K. Here and later in this paragraph the value in parentheses is the standard deviation of the mean of the Rietveld determined oxygen content at different temperatures. This value decreased on heating in a 1:1 CO_2:CO atmosphere to an average of 2.721(8) between 873 and 1093 K. This apparent oxygen loss is greater than indicated by the gas analysis (which showed the expected oxygen content of 2.793(3)). This difference between neutron scattering results and other methods for oxygen determination has been seen in other perovskite structures [31]. Given the significant number of oxygen vacancies in the reduced material, it is probable that there is local short-range ordering of vacancies, despite the average structure remaining perovskite like. It is well known, for example, that several materials that form ordered brownmillerite structures at composition $ABO_{2.5}$ have perovskite average structures at higher oxygen content or when quenched from high temperature [15]. To model short-range order, an additional oxygen site close to that expected for local tetrahedral Fe coordination was introduced. This site remained unpopulated below 623 K but became partially populated at the higher temperatures where oxygen disorder is expected. Using this treatment, total refined oxygen contents became 2.794(7) above 743 K. The corresponding oxygen loss is closer to that measured by gas analysis. Values based on this model are reported in Fig. 3.

Neutron and synchrotron data sets at high temperature under different atmospheres were analysed using a $Pm\bar{3}m$ model. Additional details of both structural models are given in the SI Section 1.

1.6. Thermogravimetric analysis

Thermogravimetric analysis was carried out on the as-synthesised material using a Rubotherm dynTHERM unit. Gas composition was controlled using Brooks flow meters. The sample consisted of 0.25 g of $La_{0.6}Sr_{0.4}FeO_{3-\delta}$ sieved to 80–160 μm and placed in the sample holder. The sample was exposed to 5% O_2 in Ar with a gas flow rate of 1.47×10^{-4} mol/s at 973 K, 1013 K, 1053 K, 1093 K, 1133 K, and 1173 K, with a heating rate of 1 K min^{-1} between each temperature.

To ensure that the sample had reached equilibrium with the gas environment, the temperature was held constant until the mass change was less than 5×10^{-4} g/min. The gas buoyancy effect on the sample was negligible, when compared with the mass changes resulting from oxygen release, so was omitted from the calculations.

2. Results

2.1. Crystal structure as a function of temperature

The rhombohedral to cubic transition of $La_{0.6}Sr_{0.4}FeO_{3-\delta}$ on heating was investigated in a reducing environment (of 1:1 CO_2:CO in Ar at atmospheric pressure, corresponding to $P_{O_2} = 1.23 \times 10^{-18}$ bar at 1093 K). The sample was heated from 298 K to 1098 K and neutron diffraction patterns collected every 25 K. Unit cell parameters as a function of temperature are shown in Fig. 3, based on a rhombohedral cell with $a = b = c = \sqrt{2}a_{cub}$ and $\alpha = \beta = \gamma \approx 60^\circ$ then converted to pseudo-cubic values. The phase transition to cubic is signified by $a_{cub} = c_{cub}$ and $\alpha = 60^\circ$. Fig. 3 shows that under this atmosphere, the rhombohedral to cubic transition occurred at approximately 750 K. The phase transition is associated with the reduction of $La_{0.6}Sr_{0.4}FeO_{3-\delta}$, and the Rietveld-refined oxygen content per formula unit at each temperature is shown in Fig. 3c. The relatively high degree of scatter is due to the short data collection times used.

2.2. Relationship between oxygen content and P_{O_2} for $La_{0.6}Sr_{0.4}FeO_{3-\delta}$

The oxygen non-stoichiometry of $La_{0.6}Sr_{0.4}FeO_{3-\delta}$ as a function of temperature in a P_{O_2} of 0.05 bar was investigated using three different methods: thermogravimetric analysis (TGA), Rietveld fitting of oxygen content from *in situ* neutron diffraction patterns, and oxygen balance calculated from the outlet gas composition measured in the same neutron diffraction experiment. These results are shown in Fig. 4 and compared to literature values [1,2,20].

The outlet gas analysis from the neutron diffraction experiment and TGA results only measure the change in δ between two states. In order to compare these results with those obtained through neutron diffraction, they are plotted relative to the degree of non-stoichiometry at 973 K of $\delta = 0.02$. This is the value derived from the δ/P_{O_2}/temperature relationship determined by Kuhn et al. [20] under the same conditions. It is worth noting that, with this assumption, the starting stoichiometry of oxygen of the as-synthesised material used in the TGA experiment was found to be 3.001 at room temperature, consistent with the expected value of 3.0 within experimental uncertainty [1,2,20].

Fig. 4 shows that the values of δ determined from the TGA, gas analysis from the neutron diffraction experiments and the predictions based on the work of Kuhn et al. [20] agree to within one standard deviation. Mizusaki et al. [1] and Søgaard et al. [2] both predict a higher value of δ than measured by the TGA or determined by Rietveld analysis. Individual values of the oxygen content from the Rietveld fitting agree with the gas analysis and TGA results, as well as the δ/P_{O_2}/temperature relationship of Kuhn et al. [20] to within the estimated uncertainty from the Rietveld fitting. However, the Rietveld values have a steeper gradient compared to other methods. This is perhaps unsurprising given the short-range order likely at higher defect levels which will affect the Rietveld results.

Fig. 5 compares δ from the three techniques with literature predictions as a function of P_{O_2} at 1093 K. The changes in δ measured from the difference between the inlet and outlet gas concentrations during the neutron diffraction studies are plotted relative to the value predicted by Kuhn et al. [20] at a P_{O_2} of 0.05 bar. The gas analysis and model results agree well with literature [20], but the values of δ from the Rietveld fits are higher by around two standard deviations. Based on these observations, the δ/P_{O_2}/temperature relationship of Kuhn et al. [20] will be used to determine the oxygen content of the material at a given temperature and P_{O_2} in all subsequent analysis.

2.3. Thermal and chemical expansivity for $\delta < 0.2$

In order to provide information on the thermal and chemical expansivity of $La_{0.6}Sr_{0.4}FeO_{3-\delta}$ in the region where $\delta < 0.2$, synchrotron XRD data were collected covering a range of P_{O_2} from 0.01 bar to 0.2 bar. This is of interest to chemical looping and chemical sensor applications [20].

Fig. 6a shows our measured unit cell parameters as a function of δ (δ calculated using the δ/P_{O_2}/temperature relationship detailed by Kuhn et al. [20]) at four different temperatures. The uncertainties in δ are dominated by the uncertainty in the pressure measurement, ±0.1 bar. As the relationship between δ and P_{O_2} is non-linear, the error bars are asymmetric. These data were used to estimate the chemical and thermal expansivity of $La_{0.6}Sr_{0.4}FeO_{3-\delta}$. The average chemical expansivity in the temperature range 930–1050 K was found to be 0.144(9) Å per unit change in δ as defined in Equation (2). This was largely independent of temperature (i.e., the lines in Fig. 6a are parallel).

In order to extract the underlying thermal expansivity, the chemical expansion was removed to obtain a pure thermal expansivity plot, Fig. 6b. This was performed by extrapolating each line in Fig. 6a to $\delta =$

a)

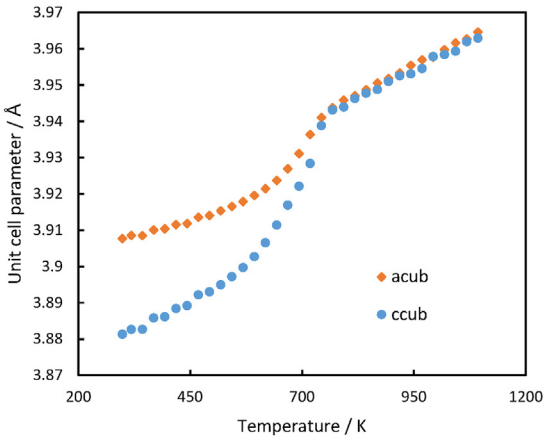

b)

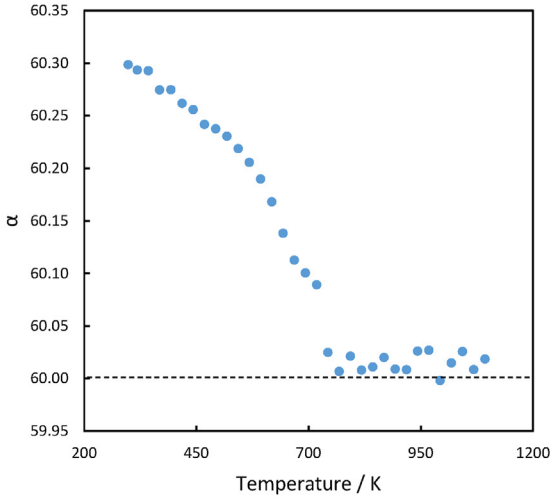

c)

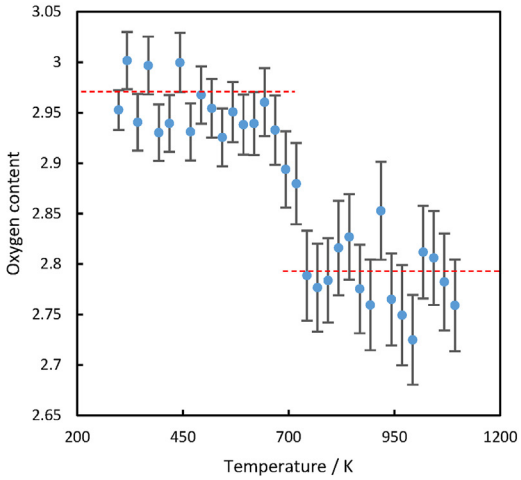

(caption on next column)

Fig. 3. Pseudo-cubic cell parameter (a), rhombohedral angle (b) and total oxygen content (c) of $La_{0.6}Sr_{0.4}FeO_{3-\delta}$ on heating in a 1:1 CO_2:CO atmosphere. In (c), the average value over different temperature ranges is denoted with a red dotted line. Error bars are one standard deviation estimated from the Rietveld fitting. The uncertainties in the unit cell parameters and rhombohedral angle are smaller than the size of the symbols. (For interpretation of the references to colour in this figure legend, the reader is referred to the Web version of this article.)

0 and gave the linear thermal expansivity as 5.70(5) $\times$ 10^{-5} Å/K. The extrapolated unit cell parameter at 0 K and $\delta = 0$ using this method was found to be 3.8741(5) Å, smaller than the value of 3.8846 Å reported by Kuhn et al. [20]. Cell parameters derived from neutron diffraction in 5% O_2 at 1 bar were used to validate the chemical and thermal expansivity; these data are shown in SI Fig. S4.

2.4. *Thermal and chemical expansivity for $\delta > 0.2$*

It is expected that the chemical and thermal expansivities of $La_{0.6}Sr_{0.4}FeO_{3-\delta}$ will be different for $\delta > 0.2$ compared to for $\delta < 0.2$, due to the presence of Fe^{2+}/Fe^{3+} ions instead of Fe^{4+}/Fe^{3+} at these lower oxygen contents [2].

As illustrated in Fig. 1, low P_{O_2} values are required to obtain $\delta > 0.2$ and redox buffers such as CO_2:CO couples or H_2O:H_2 couples are needed to maintain such low P_{O_2}. In this work, CO_2:CO redox couples were used because the reaction.

$\varepsilon CO + La_{0.6}Sr_{0.4}FeO_{3-\gamma} \rightarrow \varepsilon CO_2 + La_{0.6}Sr_{0.4}FeO_{3-\gamma-\varepsilon}$ Reaction 1

has a ΔH close to zero and consequently the equilibrium constant will not change with temperature [20,21]. As a result, the oxygen content of the perovskite should not change significantly between 973 and 1173 K for a given CO_2:CO buffer. The thermal expansivity can then be measured without the influence of the chemical expansion. This differs to the work in Section 3.3 where the P_{O_2} remains constant, leading to different δ at different temperatures. The cell parameters of $La_{0.6}Sr_{0.4}FeO_{3-\delta}$ derived from neutron diffraction data under various CO_2:CO buffers are shown in Fig. 7 (also see Table S3 from the SI). Similar to the case of $\delta < 0.2$, the thermal expansivity of $La_{0.6}Sr_{0.4}FeO_{3-\delta}$ is essentially independent of δ (Table 2). The average thermal expansivity using the data collected for all the buffer gasses was 6.18(8) $\times$ 10^{-5} Å/K, larger than the value of 5.72(4) $\times$ 10^{-5} Å/K found for $\delta < 0.2$. This indicates that two regimes of thermal expansivity exist.

The small change in unit cell parameter on switching from a 100:1 to 1:10 CO_2:CO buffer (*i.e.* to a more reducing atmosphere) is plotted as a function of calculated δ in Fig. 8a at six different temperatures, using the data of Fig. 7. It shows that the chemical expansivity is non-linear for $\delta > 0.2$, decreasing with increasing δ. The chemical expansivity also becomes dependent on temperature, with higher temperatures resulting in larger changes in unit cell parameter for the same change in δ. Furthermore, the chemical expansivity is approximately a tenth of the values found for $\delta < 0.2$. As such, for $\delta > 0.2$, the effect of the thermal expansivity is much larger than the effect of chemical expansivity in these experiments; this results in the change in unit cell parameter between the different experiments being dominated by the effect of temperature in Fig. 7.

Fitting a straight line through the curves in Fig. 8a gives an indicative linear chemical expansivity at each temperature. Using the 1093 K chemical expansivity, unit cell parameters were predicted for the small range of P_{O_2} which was studied using X-ray diffraction experiments to provide a consistency check. The comparison can be seen in SI Fig. S5.

3. Discussion

It is clear from the results presented in Section 3 that the chemical expansivity of $La_{0.6}Sr_{0.4}FeO_{3-\delta}$ changes significantly at $\delta \approx 0.2$. This gives insight into the main structural influences on the cell parameter. Assuming fixed oxidation states for La, Sr and O, the principal charge compensation on reduction is via a changing ratio of Fe^{4+} to Fe^{3+} for $0 \leq$

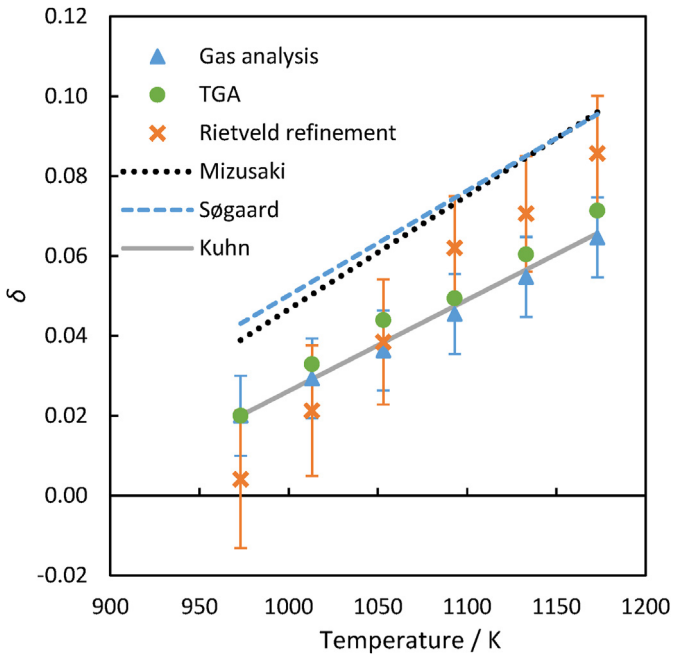

Fig. 4. δ in $La_{0.6}Sr_{0.4}FeO_{3-\delta}$ as a function of temperature at P_{O_2} = 0.05 bar calculated from the Rietveld fitting of *in situ* neutron diffraction patterns and outlet gas conditions (error bars show one standard deviation), compared to predicted values obtained from δ/P_{O_2}/temperature relationships found in the literature [1,2,20] and TGA results (standard deviations smaller than the size of the markers). The δ/P_{O_2}/temperature relationship from Mizusaki et al. [1] and Søgaard et al. [2] were extrapolated from models fitted at higher temperatures.

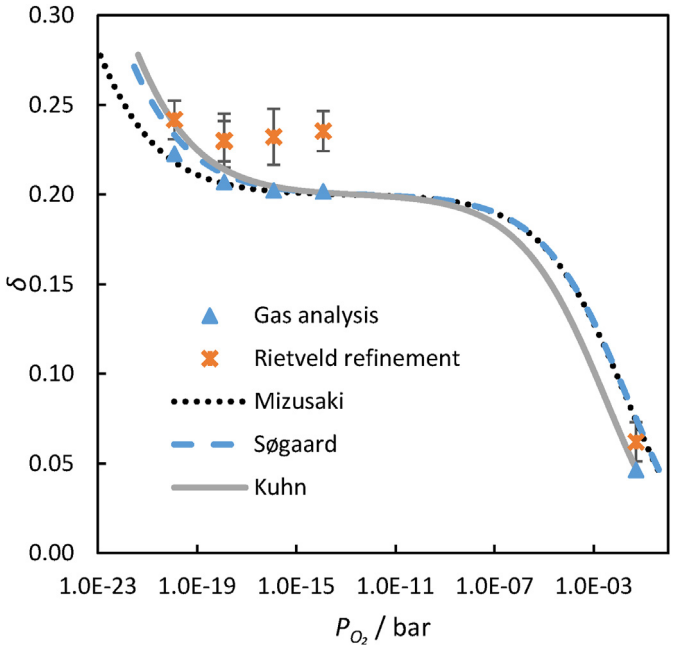

Fig. 5. δ at 1093 K calculated from Rietveld fitting of neutron diffraction data (with error bars showing one standard deviation) and from outlet gas analysis (error bars are smaller than the data points) compared to predicted values from the δ/P_{O_2}/temperature relationship in the literature [1,2,20].

$\delta \leq 0.2$ and Fe^{3+} to Fe^{2+} for $\delta \geq 0.2$ [20]. Given that the sample retains, at least on average, the cubic perovskite structure at the high temperatures studied, one might assume that the chemical expansivity would be influenced by the increasing average ionic radius of Fe on reduction (high

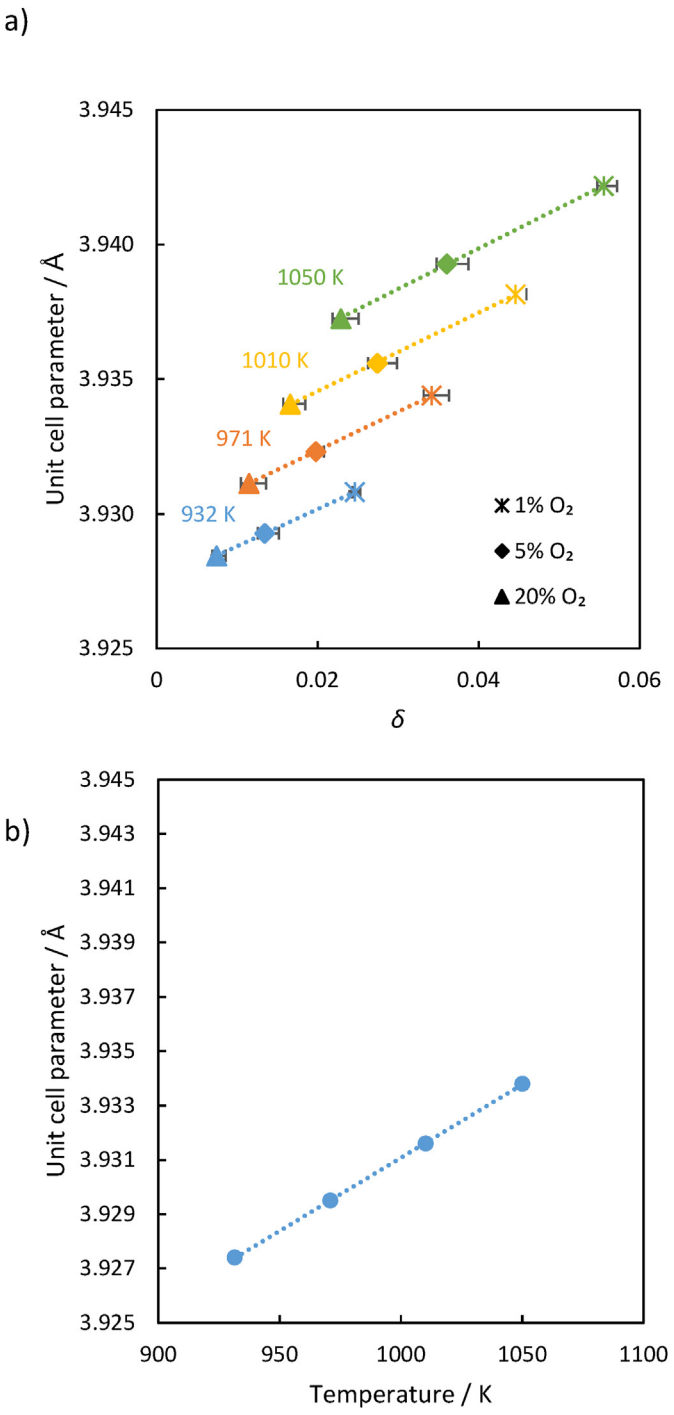

Fig. 6. a) Plot of unit cell parameter as a function of predicted δ (based on the δ/P_{O_2}/temperature relationship of *Kuhn* et al. [20]). Three different P_{O_2} were used: 1%, 5% and 20% O_2 in Ar at a total pressure of 1 bar. Lines of best fit are added for each temperature. B) Plot of predicted unit cell parameter of $La_{0.6}Sr_{0.4}FeO_{3-\delta}$ at $\delta = 0$ extrapolated from Fig. 6a, with the line of best fit $a = 5.70(5) \times 10^{-5}\ T + 3.8741(5)$. The estimated standard deviation of the unit cell parameters is smaller than the symbols.

spin radii for Fe^{4+}, Fe^{3+} and Fe^{2+} are 0.58, 0.645 and 0.78 Å, respectively [32]). Under this assumption, one might expect the chemical expansivity in the Fe^{3+} to Fe^{2+} region ($\delta > 0.2$) to be larger than in the Fe^{4+} to Fe^{3+} ($\delta < 0.2$) region, due to the larger change in ionic radii in the former case. However, the change in oxidation state of Fe occurs alongside a change in its average coordination number from 6 at $\delta = 0.0$ to 5.5 at $\delta = 0.25$. Even though the average structure remains perovskite, locally there will be a

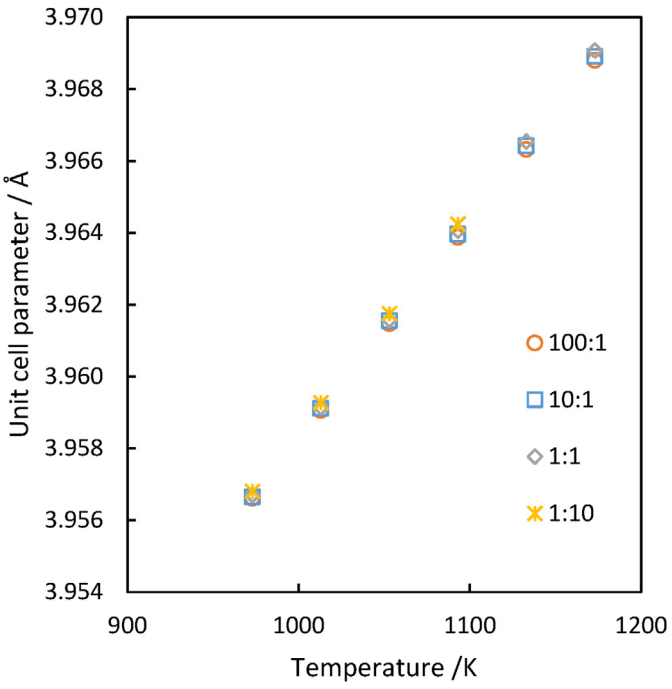

Fig. 7. Unit cell parameter of $La_{0.6}Sr_{0.4}FeO_{3-\delta}$ from neutron diffraction in 100:1, 10:1, 1:1 and 1:10 CO_2:CO buffer gasses. Error bars are smaller than the data points.

Table 2
Thermal expansivity of $La_{0.6}Sr_{0.4}FeO_{3-\delta}$ from neutron diffraction in different buffer gasses for a temperature range of 977 K–1173 K.

Gas	P_{O_2} at 1093 K (bar)	δ	Thermal expansivity (Å/K)
1:10 CO_2:CO ratio	1.23×10^{-20}	0.240	$6.20(2) \times 10^{-5}$
1:1 CO_2:CO ratio	1.23×10^{-18}	0.214	$6.18(2) \times 10^{-5}$
10:1 CO_2:CO ratio	1.23×10^{-16}	0.205	$6.11(2) \times 10^{-5}$
100:1 CO_2:CO ratio	1.23×10^{-14}	0.201	$6.08(4) \times 10^{-5}$
Various O_2 mole fractions from Section 3.3	0.05–0.20	<0.2	$5.70(5) \times 10^{-5}$

mixture of square pyramidal (as found in $Sr_8Fe_8O_{23}$ and $Sr_4Fe_4O_{11}$; δ = 0.125 and 0.25 respectively) or tetrahedral (as found in $Sr_2Fe_2O_5$; δ = 0.5) or some other coordination environment present [33].

As shown in Fig. 9, the ionic radius of a four-coordinate Fe^{2+} is comparable to six-coordinate Fe^{3+}. One would therefore see little change in local bond lengths, and therefore unit cell parameters, if this transformation occurs. We therefore conclude that the cell parameter of $La_{0.6}Sr_{0.4}FeO_{3-\delta}$ depends more on the local coordination environment than on the average oxidation state of Fe, which results in the strong non-linearity seen in Fig. 8. While Fig. 9 is based on room temperature data, similar arguments are likely to hold at high temperature. Similar observations have been made for related perovskites such as $(La,Sr)FeO_{3-\delta}$ [16], $(La,Sr)CoO_{3-\delta}$ [34], and (La,Sr) $(Co,Fe)O_{3-\delta}$, [35]. Studies on Cr and Co based perovskites also showed strong non-linear dependence on oxygen content but for these materials the expansivity was still dominated by the cation size [36,37].

4. Conclusions

In this work, the variation of the chemical and thermal expansivities of $La_{0.6}Sr_{0.4}FeO_{3-\delta}$ over the important operating P_{O_2} ranges for chemical looping and sensor applications was obtained through neutron and X-ray diffraction experiments combined with *in situ* measurement of oxygen content changes through simultaneous gas analysis. This approach

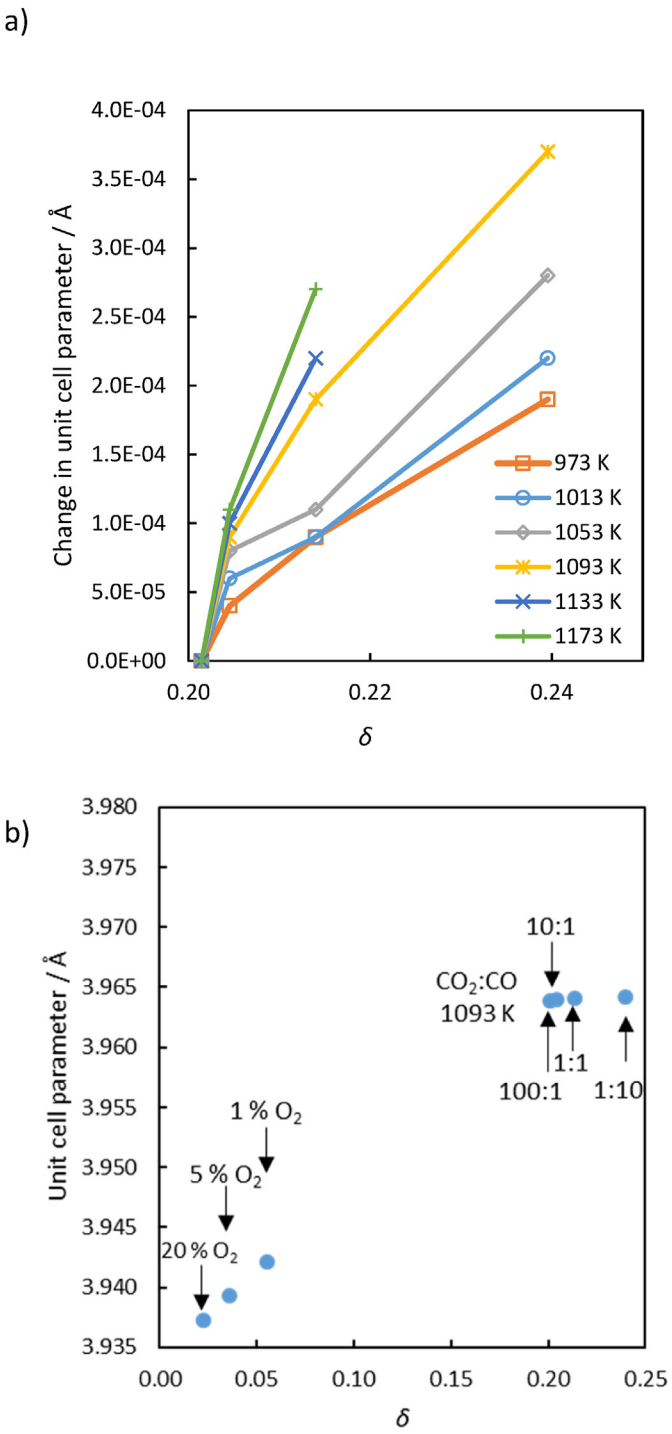

Fig. 8. a) Change in unit cell parameter relative to a δ of 0.201 calculated from *in situ* neutron diffraction as a function of calculated δ in different atmospheres. This was carried out at 973 K, 1013 K, 1053 K, 1093 K, 1133 K and 1173 K using gas atmospheres of CO_2:CO = 1:10 (δ = 0.240), 1:1 (δ = 0.214), 10:1 (δ = 0.205) and 100:1 (δ = 0.201). B) unit cell parameter at 1093 K using gas atmospheres of 1%, 5% and 20% O_2 in Ar at a total pressure of 1 bar and CO_2:CO buffers with ratio of 1:10, 1:1, 10:1 and 100:1.

provides an independent check that equilibrium conditions are reached and allows confirmation of the true change in oxygen content of samples during diffraction experiments.

The change in equilibrium δ between different conditions was determined experimentally, and calculated using literature values of the δ/P_{O_2}/temperature relationship [20]. It was found that:

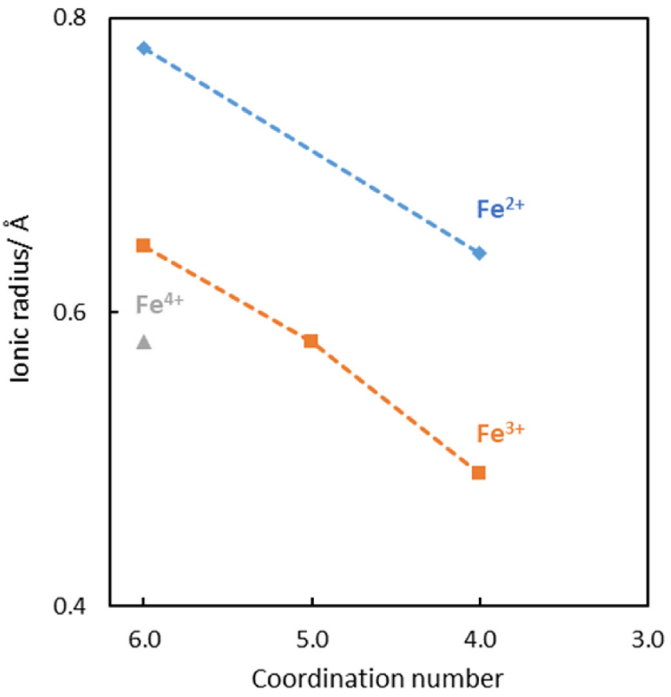

Fig. 9. High spin ionic radius of Fe ions as a function of coordination number and oxidation state [32].

1. For $\delta < 0.2$ and in the temperature range 932–1050 K, the chemical expansivity is 0.144(9) Å per unit change in δ. This is larger than the value of 0.07773 Å reported by Kuhn et al. [20].
2. For $\delta < 0.2$ and in the temperature range 932–1050 K, the thermal expansivity is 5.72(4) $\times$ 10^{-5} Å/K. This compares with a value of 4.037 $\times$ 10^{-5} Å/K reported by Kuhn et al. [20].
3. For $\delta > 0.2$ and in the temperature range 973–1173 K, the chemical expansivity varies with both δ and temperature. Chemical expansivity decreases with increasing δ and increases with increasing temperature. However, regardless of the value of δ, the chemical expansivity in this regime is smaller than that determined for $\delta < 0.2$.
4. For $\delta > 0.2$ and in the temperature range 973–1173 K, the thermal expansivity is 6.18(8) $\times$ 10^{-5} Å/K.

Declaration of competing interest

The authors declare that they have no known competing financial interests or personal relationships that could have appeared to influence the work reported in this paper.

Acknowledgement

We gratefully acknowledge the Science and Technology Facilities Council (STFC) for access to neutron beamtime (HRPD) at ISIS. The synchrotron experiments were performed on beamline ID22 at the European Synchrotron Radiation Facility (ESRF), Grenoble, France. We are grateful to Andy Fitch and Catherine Dejoie for providing assistance in using beamline ID22. The research leading to these results has received funding from the European Research Council under the European Union's Seventh Framework Programme (FP/2007–2013)/ERC grant agreement no. 320725 and from the EPSRC via grants EP/P007767/1 and EP/P024807/1. CdL thanks EPSRC for funding via a doctoral training award.

Appendix A. Supplementary data

Supplementary data to this article can be found online at https://doi.org/10.1016/j.jssc.2020.121838.

References

[1] J. Mizusaki, M. Yoshihiro, S. Yamauchi, K. Fueki, Nonstoichiometry and defect structure of the perovskite-type oxides $La_{1-x}Sr_xFeO_{3-\delta}$, J. Solid State Chem. 58 (1985) 257–266, https://doi.org/10.1016/0022-4596(85)90243-9.
[2] M. Søgaard, P. Vang Hendriksen, M. Mogensen, Oxygen nonstoichiometry and transport properties of strontium substituted lanthanum ferrite, J. Solid State Chem. 180 (2007) 1489–1503, https://doi.org/10.1016/j.jssc.2007.02.012.
[3] D. Bayraktar, S. Diethelm, T. Graule, J. Van Herle, P. Holtappels, Properties of B-site substituted $La_{0.5}Sr_{0.5}FeO_{3-\delta}$ perovskites for application in oxygen separation membranes, J. Electroceram. 22 (2009) 55–60, https://doi.org/10.1007/s10832-008-9428-z.
[4] U.F. Vogt, P. Holtappels, J. Sfeir, J. Richter, S. Duval, D. Wiedenmann, L. Zütte, Influence of A-site variation and B-site substitution on the physical properties of (La,Sr)FeO_3 based perovskites, Fuel Cell. 9 (2009) 899–906, https://doi.org/10.1002/fuce.200800116.
[5] J.E. ten Elshof, Oxygen exchange and diffusion coefficients of strontium-doped lanthanum ferrites by electrical conductivity relaxation, J. Electrochem. Soc. 144 (1997) 1060, https://doi.org/10.1149/1.1837531.
[6] H. Obayashi, T. Kudo, N. Kaishi, Properties of oxygen deficient perovskite type compounds and their application as alcohol sensors, Nippon Kagaku Kaishi (1980) 1568–1572.
[7] T. Arakawa, H. Kurachi, J. Shiokawa, Physicochemical properties of rare earth perovskite oxides used as gas sensor material, J. Mater. Sci. 20 (1985) 1207–1210, https://doi.org/10.1007/BF01026315.
[8] E. Traversa, S. Matsushima, G. Okada, Y. Sadaoka, Y. Sakai, K. Watanabe, NO_2 sensitive $LaFe_3$ thin films prepared by r.f. sputtering, Sensor. Actuator. B Chem. 25 (1995) 661–664, https://doi.org/10.1016/0925-4005(95)85146-1.
[9] L.S. Fan, Chemical Looping Systems for Fossil Energy Conversions, John Wiley and Sons, 2010, https://doi.org/10.1002/9780470872888.
[10] J. Adanez, A. Abad, F. Garcia-Labiano, P. Gayan, L.F. De Diego, Progress in chemical-looping combustion and reforming technologies, Prog. Energy Combust. Sci. 38 (2012) 215–282, https://doi.org/10.1016/j.pecs.2011.09.001.
[11] D.D. Taylor, N.J. Schreiber, B.D. Levitas, W. Xu, P.S. Whitfield, E.E. Rodriguez, Oxygen storage properties of $La_{1-x}Sr_xFeO_{3-\delta}$ for chemical-looping reactions—an in situ neutron and synchrotron X-ray study, Chem. Mater. 28 (2016) 3951–3960, https://doi.org/10.1021/acs.chemmater.6b01274.
[12] I. Dincer, C. Acar, Review and evaluation of hydrogen production methods for better sustainability, Int. J. Hydrogen Energy 40 (2014) 11094–11111, https://doi.org/10.1016/j.ijhydene.2014.12.035.
[13] S.R. Bishop, D. Marrocchelli, C. Chatzichristodoulou, N.H. Perry, M.B. Mogensen, H.L. Tuller, E.D. Wachsman, Chemical expansion: implications for electrochemical energy storage and conversion devices, Annu. Rev. Mater. Res. 44 (2014) 205–239, https://doi.org/10.1146/annurev-matsci-070813-113329.
[14] M. Rydén, A. Lyngfelt, T. Mattisson, D. Chen, A. Holmen, E. Bjørgum, Novel oxygen-carrier materials for chemical-looping combustion and chemical-looping reforming; $La_xSr_{1-x}Fe_yCo_{1-y}O_{3-\delta}$ perovskites and mixed-metal oxides of NiO, Fe_2O_3 and Mn_3O_4, Int. J. Greenh. Gas Control 2 (2008) 21–36, https://doi.org/10.1016/S1750-5836(07)00107-7.
[15] S.E. Dann, D.B. Currie, M.T. Weller, M.F. Thomas, A.D. Al-Rawwas, The effect of oxygen stoichiometry on phase relations and structure in the system $La_{1-x}Sr_xFeO_{3-\delta}$ ($0 \le x \le 1$, $0 \le \delta \le 0.5$), J. Solid State Chem. 109 (1994) 134–144, https://doi.org/10.1006/jssc.1994.1083.
[16] X. Chen, T. Grande, Anisotropic and nonlinear thermal and chemical expansion of $La_{1-x}Sr_xFeO_{3-\delta}$ ($x = 0.3, 0.4, 0.5$) perovskite materials, Chem. Mater. 25 (2013) 3296–3306, https://doi.org/10.1021/cm401100c.
[17] A. Fossdal, M. Menon, I. Waernhus, K. Wiik, M.-A. Einarsrud, T. Grande, Crystal structure and thermal expansion of $La_{1-x}Sr_xFeO_{3-\delta}$ materials, J. Am. Ceram. Soc. 87 (2005) 1952–1958, https://doi.org/10.1111/j.1151-2916.2004.tb06346.x.
[18] D. Gryaznov, R. Merkle, E.A. Kotomin, J. Maier, Ab initio modelling of oxygen vacancies and protonic defects in $La_{1-x}Sr_xFeO_{3-\delta}$ perovskite solid solutions, J. Mater. Chem. A. 4 (2016) 13093–13104, https://doi.org/10.1039/c6ta04109d.
[19] T. Götsch, L. Schlicker, M.F. Bekheet, A. Doran, M. Grünbacher, C. Praty, M. Tada, H. Matsui, N. Ishiguro, A. Gurlo, B. Klötzer, S. Penner, Structural investigations of $La_{0.6}Sr_{0.4}FeO_{3-\delta}$ under reducing conditions: kinetic and thermodynamic limitations for phase transformations and iron exsolution phenomena, RSC Adv. 8 (2018) 3120–3131, https://doi.org/10.1039/c7ra12309d.
[20] M. Kuhn, S. Hashimoto, K. Sato, K. Yashiro, J. Mizusaki, Oxygen nonstoichiometry, thermo-chemical stability and lattice expansion of $La_{0.6}Sr_{0.4}FeO_{3-\delta}$, Solid State Ionics 195 (2011) 7–15, https://doi.org/10.1016/j.ssi.2011.05.013.
[21] D. Burgess, Thermochemical data, in: P. Linstrom, W. Mallard (Eds.), NIST Chem. WebBook, NIST Stand. Ref. Database Number 69, National Institute of Standards and Technology, Gaithersburg MD, 2019, p. 20899, https://doi.org/10.18434/T4D303.
[22] L. Dimesso, Pechini processes: an alternate approach of the sol–gel method, preparation, properties, and applications, in: Handb. Sol-Gel Sci. Technol, Springer International Publishing, 2016, pp. 1–22, https://doi.org/10.1007/978-3-319-19454-7_123-1.
[23] ISIS High Temperature Furnaces. https://www.isis.stfc.ac.uk/Pages/High-Temperature-Furnaces.aspx. (Accessed 18 August 2020).
[24] I.S. Metcalfe, B. Ray, C. Dejoie, W. Hu, C. de Leeuwe, C. Dueso, F.R. García-García, C.M. Mak, E.I. Papaioannou, C.R. Thompson, J.S.O. Evans, Overcoming chemical

equilibrium limitations using a thermodynamically reversible chemical reactor, Nat. Chem. 11 (2019) 638–643, https://doi.org/10.1038/s41557-019-0273-2.
[25] V. Swamy, H.J. Seifert, F. Aldinger, Thermodynamic properties of Y2O3 phases and the yttrium-oxygen phase diagram, J. Alloys Compd. 269 (1998) 201–207, https://doi.org/10.1016/S0925-8388(98)00245-X.
[26] J.-L. Hodeau, P. Bordet, M. Anne, A. Prat, A.N. Fitch, E. Dooryhee, G. Vaughan, A.K. Freund, Nine-crystal multianalyzer stage for high-resolution powder diffraction between 6 keV and 40 keV, Cryst, Multilayer Opt 3448 (1998) 353, https://doi.org/10.1117/12.332525.
[27] V. Swamy, N.A. Dubrovinskaya, L.S. Dubrovinsky, High-temperature powder x-ray diffraction of yttria to melting point, J. Mater. Res. 14 (1999) 456–459, https://doi.org/10.1557/JMR.1999.0065.
[28] D. Taylor, Thermal expansion data : III sesquioxides, M_2O_3, with the corundum and the A-, B- and C-M_2O_3 structures, Trans. J. Br. Ceram. Soc. 83 (1984) 92.
[29] A. Coelho, TOPAS Academic: General Profile and Structure Analysis Software for Powder Diffraction Datale, fifth ed., 2012. Karlsruhe, Germany.
[30] R.E. Dinnebier, A. Leineweber, J.S.O. Evans, Rietveld Refinement: Practical Powder Diffraction Pattern Analysis Using TOPAS, first ed., De Gruyter, Berlin Boston, 2019 https://doi.org/10.1515/9783110461381.
[31] A.A. Yaremchenko, D.D. Khalyavin, M.V. Patrakeev, Uncertainty of oxygen content in highly nonstoichiometric oxides from neutron diffraction data: example of perovskite-type $Ba_{0.5}Sr_{0.5}Co_{0.8}Fe_{0.2}O_{3-\delta}$, J. Mater. Chem. A. 5 (2017) 3456–3463, https://doi.org/10.1039/c6ta10236k.
[32] R.D. Shannon, Revised effective ionic radii and systematic studies of interatomic distances in halides and chalcogenides, Acta Crystallogr. A 32 (1976) 751–767, https://doi.org/10.1107/S0567739476001551.
[33] J.P. Hodges, S. Short, J.D. Jorgensen, X. Xiong, B. Dabrowski, S.M. Mini, C.W. Kimball, Evolution of oxygen-vacancy ordered crystal structures in the perovskite series $Sr_nFe_nO_{3n-1}$ (n = 2, 4, 8, and ∞), and the relationship to electronic and magnetic properties, J. Solid State Chem. 151 (2000) 190–209, https://doi.org/10.1006/jssc.1999.8640.
[34] X. Chen, J. Yu, S.B. Adler, Thermal and chemical expansion of Sr-doped lanthanum cobalt oxide ($La_{1-x}Sr_xCoO_{3-\delta}$), Chem. Mater. 17 (2005) 4537–4546, https://doi.org/10.1021/cm050905h.
[35] A.Y. Zuev, V.V. Sereda, D.S. Tsvetkov, Defect structure and defect-induced expansion of doped perovskite $La_{0.7}Sr_{0.3}Co_{0.9}Fe_{0.1}O_{3-\delta}$, Int. J. Hydrogen Energy 39 (2014) 21553–21560, https://doi.org/10.1016/j.ijhydene.2014.09.115.
[36] A.Y. Zuev, A.I. Vylkov, A.N. Petrov, D.S. Tsvetkov, Defect structure and defect-induced expansion of undoped oxygen deficient perovskite $LaCoO_{3-\delta}$, Solid State Ionics 179 (2008) 1876–1879, https://doi.org/10.1016/j.ssi.2008.06.001.
[37] P.H. Larsen, P.V. Hendriksen, M. Mogensen, Dimensional stability and defect chemistry of doped lanthanum chromites, J. Therm. Anal. 49 (1997) 1263–1275, https://doi.org/10.1007/BF01983683.